Strain-Controlled Low-Cycle Fatigue Behavior of Friction Stir-Welded AZ31 Magnesium Alloy

J. YANG, D.R. NI, D. WANG, B.L. XIAO, and Z.Y. MA

Strain-controlled low-cycle fatigue (LCF) behavior of friction stir-welded (FSW) AZ31 joints, produced at rotation rates of 800 and 3500 rpm, was studied. The joints exhibited symmetric hysteresis loops, whereas asymmetric loops were observed for the parent material (PM). The fatigue resistance of the FSW joints was slightly improved as the rotation rate increased, and both the FSW joints possessed a fatigue life similar to that of the PM at the low strain amplitude of 0.1 pct. The obtained fatigue data for the PM and FSW joints can be well described using the Coffin–Manson and Basquin's relationships. For the FSW joints, during LCF deformation, the $\{10\bar{1}2\}$ twinning originated from the nugget zone (NZ)/thermomechanically affected zone (TMAZ) boundary and then propagated to the NZ interior. This was attributed to different textures in these regions: the center of the NZ exhibited a hard orientation, whereas a soft orientation was observed in the region around the NZ/TMAZ boundary. The fatigue cracks initiated at the bottom of the joints and propagated along the NZ/TMAZ boundary or the NZ adjacent to the NZ/TMAZ boundary.

I. INTRODUCTION

MAGNESIUM (Mg) alloys are very attractive candidates for structural applications in the aerospace and automobile industries because of their weight reduction and energy saving characteristics. Therefore, a reliable welding process is urgently required to realize these applications, especially for the wrought Mg alloys. However, conventional fusion welding methods have some problems for the welding of Mg alloys such as porosity, oxidization, and high residual stress. Friction stir welding (FSW), as a solid joining method[1] can effectively avoid the drawbacks of the fusion welding, producing sound joints of Mg alloys.

As a widely used wrought Mg alloy with a good combination of strength and ductility, AZ31 has been widely subjected to FSW investigations, including studies of the texture distribution,[2–4] precipitation,[5] material flow,[6,7] residual stress,[8] and mechanical properties.[9–14] It was reported that high-quality FSW AZ31 joints with excellent mechanical properties could be obtained by optimizing the welding parameters.[9,15]

From an engineering design perspective, it is important to understand the fatigue behavior of FSW joints. Recently, some studies have evaluated the fatigue resistance of FSW AZ31 joints, including the behavior of stress-controlled failure[16–18] and fatigue crack propagation.[19] Padmanaban et al.[18,19] found that FSW AZ31 joints had a higher fatigue strength and lower fatigue crack growth exponent than the joints formed by pulsed current gas tungsten arc welding. Chowdhury et al.[17] reported that the fatigue strength of FSW AZ31 joints was affected by the pin thread orientation. However, investigations into the low-cycle fatigue (LCF) behavior of FSW AZ31 joints, which is of practical importance in estimating the component lifetime during the service process,[20,21] are lacking.

It is well documented that wrought Mg alloys have strong textures. For FSW Mg alloy joints, it was reported that the intense material flow during FSW generated a special texture distribution in the nugget zone (NZ), with the basal plane rotating around the pin column surface.[2,3] This texture distribution influenced the tensile properties[14,22] and fracture behavior[10,23] of the FSW Mg alloy joints. For example, the ultimate tensile strength (UTS) of FSW AZ31 joints increased as the rotation rate increased, attributable to the texture variation.[22] Furthermore, it was reported that FSW AZ31 and AZ61 joints failed in the thermomechanically affected zone (TMAZ) during the tensile test because of the soft orientation of this region.[10,22] However, the effect of the texture distribution on the LCF properties of the FSW Mg alloy joints is still unclear.

In this study, FSW AZ31 joints produced at lower and higher rotation rates of 800 and 3500 rpm were subjected to LCF investigation. The objectives are (a) to elucidate the cyclic deformation characteristics of the joints and the microstrucural evolution during the cyclic deformation, and (b) to identify the effect of rotation rate and texture distribution on the LCF properties of the joints.

J. YANG, formerly Postgraduate with Shenyang National Laboratory for Materials Science, Institute of Metal Research, Chinese Academy of Sciences, 72 Wenhua Road, Shenyang 110016, People's Republic of China, is now Postdoctoral Fellow with the University of Science and Technology Beijing, 30 Xueyuan Road, Beijing 10083, People's Republic of China. D.R. NI, Associate Professor, D. WANG, Assistant Professor, and B.L. XIAO and Z.Y. MA, Professors, are with the Shenyang National Laboratory for Materials Science, Institute of Metal Research, Chinese Academy of Sciences. Contact e-mail: zyma@imr.ac.cn

II. EXPERIMENTAL

6.4-mm-thick commercial AZ31 rolled plates were friction stir welded along the rolling direction (RD). The welding tool was fabricated from a tool steel and consisted of a concave shoulder 24 mm in diameter and an M8 cylindrical threaded pin 6.1 mm in length. The welding speed was fixed at 100 mm min^{-1}, and two rotation rates of 800 and 3500 rpm were selected. Three directions of the rolled plate were named as the normal direction (ND), the transverse direction (TD), and the RD, respectively, as shown in Figure 1.

The specimens for microstructural examination were cross sectioned perpendicular to the welding direction. Microstructural characterization was carried out using optical microscopy, scanning electron microscopy (SEM, Hitachi S-3400N), and electron backscattered diffraction (EBSD, HKL). The specimens for EBSD analyses were prepared by electrochemical polishing with 50 ml perchloric acid + 450 ml alcohol at 243 K (−30 °C).

Transverse tensile specimens with a gauge length of 40 mm and a gage width of 10 mm were machined perpendicular to the welding direction, and tested at a strain rate of 1×10^{-3} s^{-1} by means of a Zwick/Roell Z050 tester. The results of tensile tests were taken from three or four specimens.

Fatigue specimens referring to ASTM E8 standard, with a parallel section of $32 \times 5.9 \times 5.8$ mm in size, were machined perpendicular to the welding direction. The specimens were ground with SiC papers up to grit 2000 to achieve a consistent, smooth surface. Total strain-controlled, push–pull type LCF tests were conducted using a computerized Instron 8863 fatigue tester. The strain was measured using an extensometer with a gage length of 25 mm. In the fatigue testing, a triangular waveform with a strain ratio of $R = -1$ was applied at a constant strain rate of 1×10^{-2} s^{-1}. The strain-controlled testing at low total strain amplitudes was operated until 10^4 cycles, then it was changed to a load-controlled test at a frequency of 35 Hz. LCF tests were conducted at total strain amplitudes of 0.1, 0.2, 0.3, 0.4, and 0.6 pct with at least two specimens being tested at

each level of strain amplitudes. After the fatigue test, the microstructures of failed samples were examined by EBSD, and the fracture surfaces were observed using an SEM (Quanta-600).

III. RESULTS AND DISCUSSION

A. Microstructure and Tensile Properties

Figure 1 shows the cross-sectional images of the FSW AZ31 joints at different rotation rates. It is clear that defect-free joints were obtained at lower and higher rotation rates of 800 and 3500 rpm. Three microstructural zones, the NZ, TMAZ, and heat-affected zone (HAZ) were identified in the cross sections of the joints. A basin-shaped nugget with about a 45 deg angle between the TD and the NZ/TMAZ boundary was obtained in the joint produced at 800 rpm (hereafter denoted as the 800-rpm joint, Figure 1(a)). A two-layer-structured NZ, which is denoted as the upper NZ and lower NZ, was observed in the joint produced at 3500 rpm (hereafter denoted as the 3500-rpm joint, Figure 1(b)). The formation mechanism of the two-layer-structured NZ has been discussed in detail in our previous study.[22]

The OM examinations indicated that the parent material (PM) exhibited inhomogeneous grains and numerous twins, which are the typical microstructures of the as-rolled Mg alloys (Figure 2(a)). The NZ of the 800-rpm joint and the lower NZ of the 3500-rpm joint were characterized by equiaxed grains (Figures 2(b) and (d)), indicating the occurrence of dynamic recrystallization.[10,14,22] However, the grains in the upper NZ of the 3500-rpm joint were nonuniform and elongated along the TD (Figure 2(c)). This is attributed to the enhancement of the shoulder effect at higher rotation rates and has been discussed in our previous study.[22]

EBSD inverse pole figure maps in the different regions of the 800-rpm joint are shown in Figures 3(a) and (c). In this joint, the grain orientation varied significantly from the middle of the NZ to the TMAZ, forming a column-distributed basal texture.[2,3] In the middle of the NZ, a similar grain orientation was observed between the coarse and fine grains (Figure 3(a)). On the NZ/TMAZ boundary, the grain orientation changed significantly from the NZ side to the TMAZ side, with the grain orientation centralized in the former and dispersed in the latter (Figure 3(c)), which could be attributed to the different degrees of plastic deformation[24] and specific deformation characteristics of the grains[7] during FSW. In addition, the grains in the NZ side were obviously larger than those in the TMAZ side (Figure 3(c)), which could be attributed to the higher temperature in the NZ.[25]

As shown in Figures 3(b) and (d), the variation of grain orientation in the joint also caused differences in the Schmid factor for basal slip. Because of the shearing effect, the basal plane was rotated around the pin column surface. In the NZ middle, the c-axis of the grains was roughly perpendicular to the TD and thus,
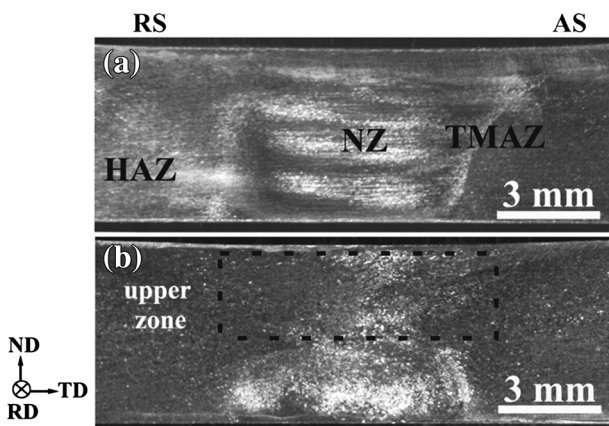
Fig. 1—Macroscopic images of transverse cross sections of FSW AZ31 joints at (a) 800 rpm and (b) 3500 rpm (the advancing side is on the right).
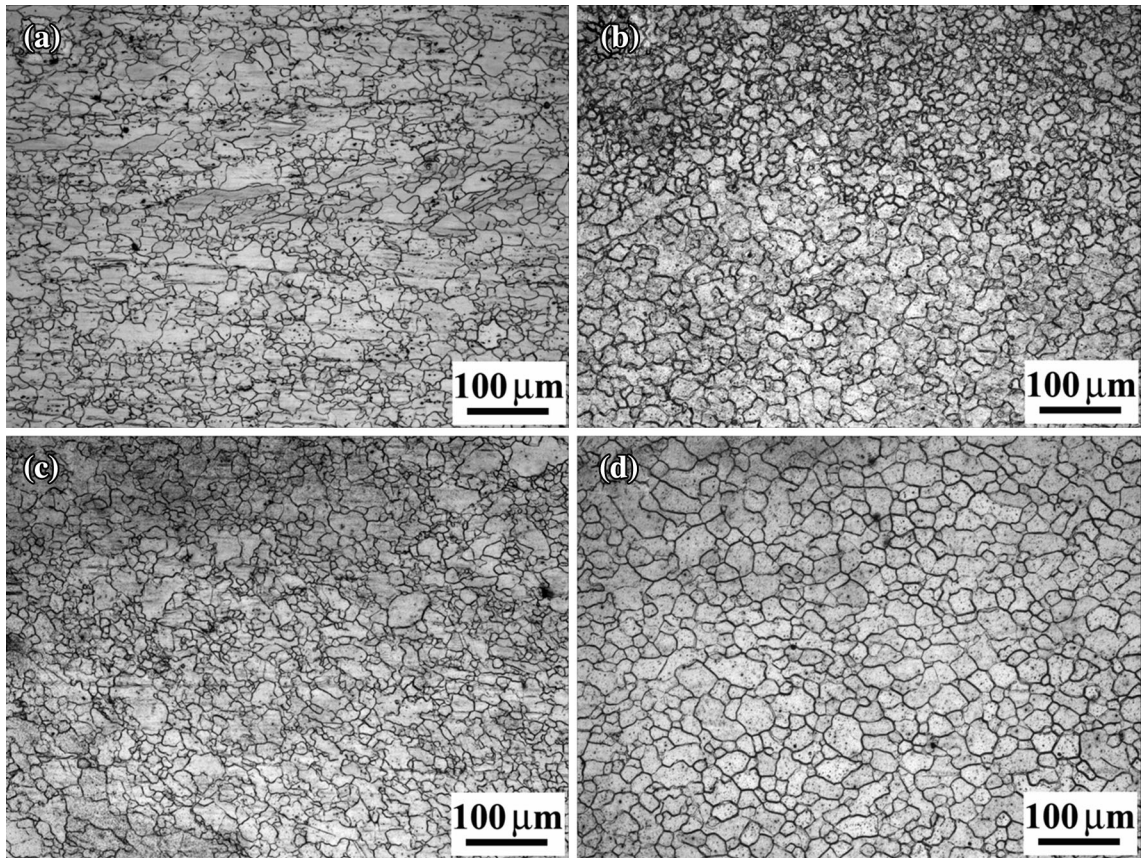
Fig. 2—OM images of FSW AZ31 joints: (*a*) PM, (*b*) NZ of 800-rpm joint, (*c*) and (*d*) the upper NZ zone and lower NZ zone of 3500-rpm joint.
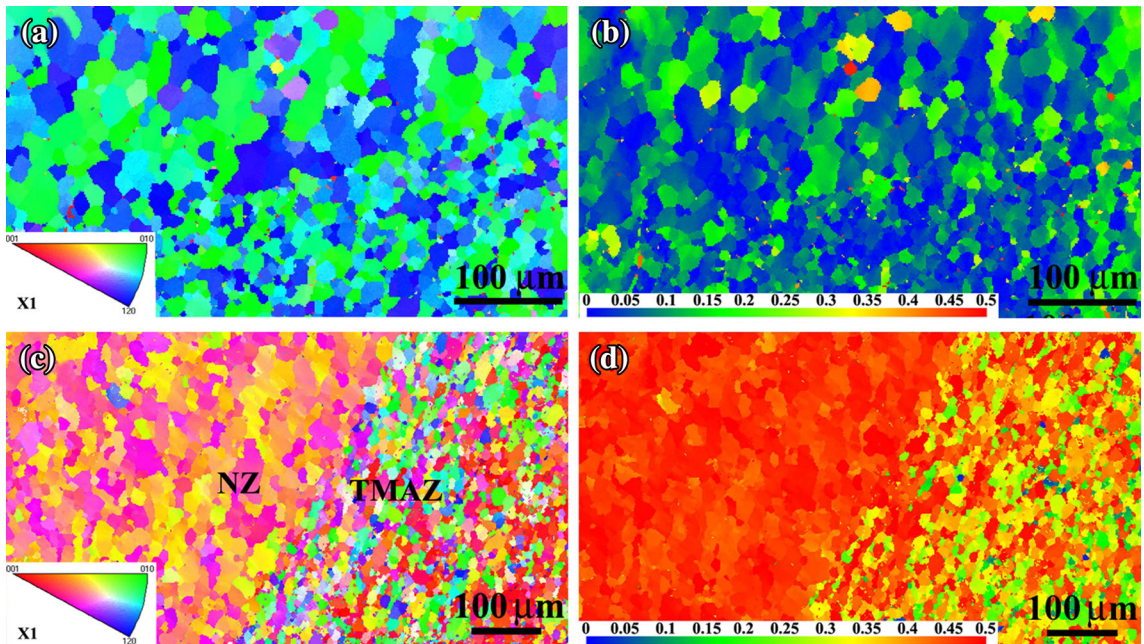
Fig. 3—EBSD inverse pole figure maps of (*a*) NZ and (*c*) NZ/TMAZ boundary; maps of Schmid factor for basal slip at (*b*) NZ and (*d*) NZ/TMAZ boundary for 800-rpm joint.

most grains had the Schmid factor in the range of 0 to 0.2 (Figure 3(b)). These orientations are not favorable for basal slip and therefore could be defined as "hard orientations."[26] On the NZ/TMAZ boundary (Figure 3(d)), the *c*-axis of the grains was tilted to the TD, and the Schmid factor was centralized in ranging from

0.4 to 0.5 on the NZ side and dispersed from 0 to 0.5 on the TMAZ side, which was consistent with the grain orientation distribution (Figure 3(c)). Therefore, the grain orientations in the NZ side are favorable for basal slip, and could be defined as "soft orientations."[26]

As the rotation rate increased to 3500 rpm, the area of the upper NZ enlarged significantly, and the grain orientation (Figure 4) was different from that in the NZ middle of the 800-rpm joint. First, the grain orientation was more dispersive. Second, the c-axis of the grains was not perpendicular to the TD, but tilted by a few degrees compared with the PM, indicating that the column-rotated basal texture was not detected in the upper NZ. However, the grain orientation in the lower NZ of the 3500-rpm joint was similar to that in the NZ of the 800-rpm joint (not shown). Clearly, the upper and lower NZs of the 3500-rpm joint had different grain orientations, which could be attributed to the different deformation mechanisms.[22]

The yield strength (YS) and ultimate tensile strength (UTS) of the PM and FSW joints are shown in Table I. Both the YS and UTS of the joints were lower than those determined for the PM, which could be attributed to the specific texture distribution in the FSW AZ31 joints.[2,23] Similar to previous studies,[14,22] the YS and UTS increased as the rotation rate increased, which was attributed to the enhancement of the upper NZ at higher rotation rates.[22] The joint efficiency (UTS_{joint}/UTS_{PM}) was about 70 pct at 800 rpm and increased to about 85 pct at 3500 rpm. It should be noted that, because different rolled AZ31 plates were used, the strength of the joints in this study was lower than that in our previous study.[22] However, the characteristics of the microstructure and the variation trend of the tensile strength were similar to those in the previous study.[22]

Similar to the previous study,[22] the NZ of the 800-rpm joint and the lower NZ of the 3500-rpm joint in this study, had a similar texture distribution, which is the typical texture distribution of FSW AZ31 joints and has been reported by several researchers.[3,7] Although a different texture was detected in the upper NZ of the 3500-rpm joint, this texture only had a strong effect at higher rotation rates with the improvement of tensile strength.[22] Therefore, the texture evolution during the fatigue deformation was discussed in detail for the 800-rpm joint in this study.

B. Microstructure of Fatigued Samples

The microstructures of the joints fatigued at different strain amplitudes are shown in Figures 5 and 6. At a strain amplitude of 0.1 pct, twins aggregated to form bands at the NZ/TMAZ boundary and adjacent NZ (Figure 5(a)), which are similar to the shear band in wrought Mg alloys.[27,28] Previous studies pointed out that double twins or $\{10\bar{1}1\}$ twins were related to the shear band formation during rolling and compression processes.[27–29] In the current study, $\{10\bar{1}2\}$ twinning bands were detected (marked by blue lines in Figures 5(b) and (c)), which could cause large local stress concentration like shear bands. Besides, these twins were continuously distributed, which could be related to the twinning distortion under macro stress.[27] On the NZ/TMAZ boundary, nonuniform deformation was caused because of the different Schmid factors and grain size distributions of the two sides (Figures 3(c) and (d)), resulting in the twinning formation. In the adjacent NZ, for the large Schmid factor (~0.5 pct), more basal slip was activated, which resulted in the formation of $\{10\bar{1}2\}$ twins because of the higher deformation degree. Moreover, there were two types of twinning band distributions in these regions. Some twinning bands were continuously distributed along the ND around the NZ/TMAZ boundary, while others were discontinuously distributed along the TD from the boundary to the NZ interior. These twinning bands were not observed during the uniaxial tension[22,30] and should be attributed to the cyclic deformation. However, because of the low stress amplitude and the hard orientation, the microstructure in the NZ middle had little variation compared with the original (not shown).

At a higher strain amplitude of 0.4 pct, except for the twinning on the NZ/TMAZ boundary, some $\{10\bar{1}2\}$ twins were observed in the NZ middle, as marked by blue lines in Figure 6. As the strain amplitude increased, the stress to activate the dislocation slip and twinning was increased, and the plastic deformation degree clearly increased (this will be discussed in Section III–C). Therefore, both the dislocation slip and twinning could be activated. Moreover, $\{10\bar{1}2\}$ twins were still distributed along the ND in the NZ middle.

As shown in Figures 1, 2, 3, and 4, the grain size and orientation had large differences in various regions of the joints, which influenced the microstructural evolution during cyclic deformation. $\{10\bar{1}2\}$ twins could arise at the NZ/TMAZ boundary and adjacent NZ at low strain amplitudes because of the soft orientation and nonuniform deformation, while it could be only observed in the NZ middle at high-strain amplitudes because of the hard orientation. This indicates that
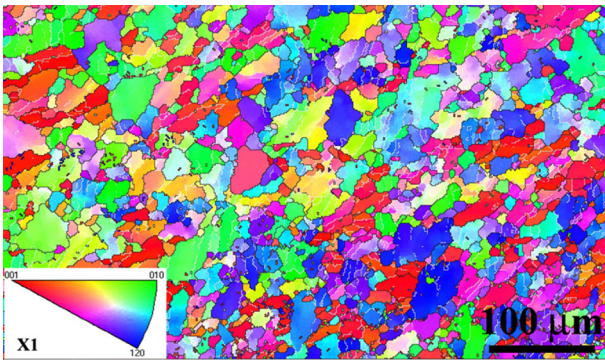
Fig. 4—EBSD inverse pole figure maps of upper NZ zone of 3500-rpm joint.

Table I. Tensile Strengths of PM and FSW Joints

	PM	800-rpm Joint	3500-rpm Joint
UTS (MPa)	275 ± 2	192 ± 2	233 ± 1
YS (MPa)	240 ± 2	115 ± 1	126 ± 1
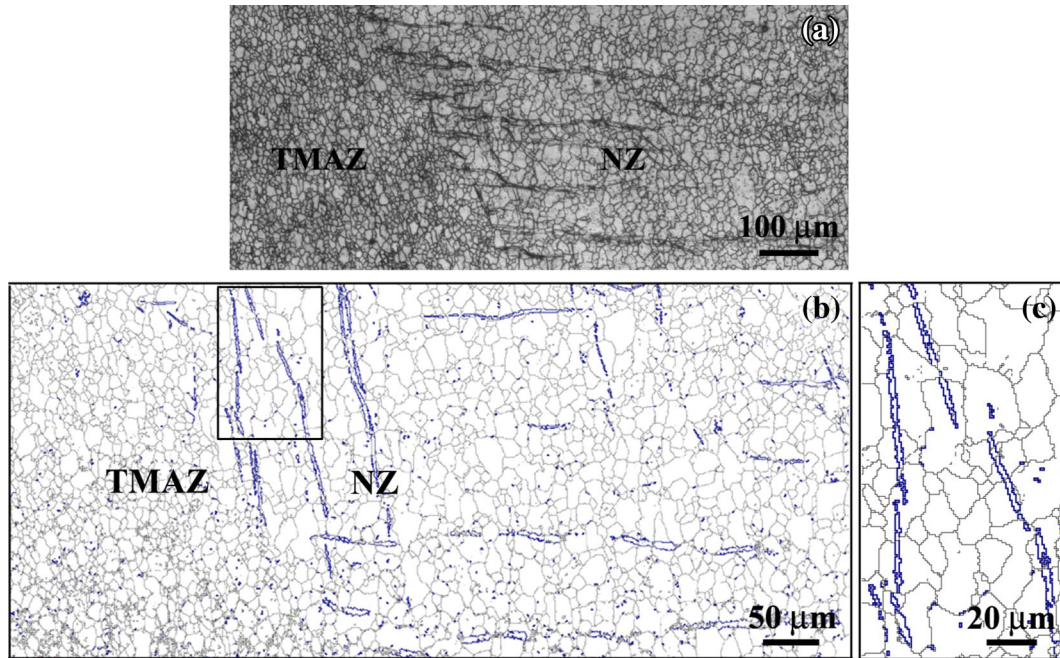
Fig. 5—Microstructures at NZ/TMAZ boundary for 800-rpm joint at a strain amplitude of 0.1 pct: (*a*) optical images, (*b*) EBSD image with twin boundaries 86 deg $\langle 1\bar{2}10 \rangle \pm 5$ deg marked by blue lines, (*c*) higher magnification of lined frame in (b).
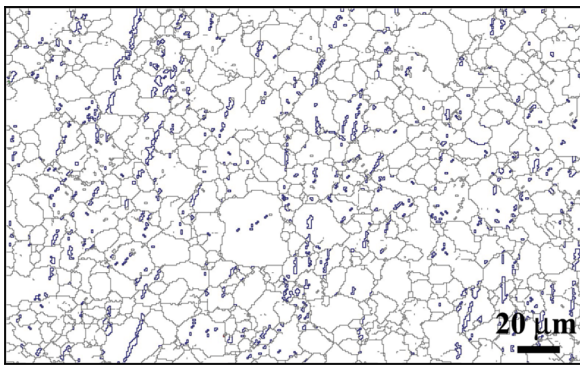
Fig. 6—EBSD images of 800-rpm joint in NZ middle with twin boundaries 86 deg $\langle 1\bar{2}10 \rangle \pm 5$ deg marked by blue lines, $\Delta\varepsilon_t/2 = 0.4$ pct.

plastic deformation could occur in the region around the NZ/TMAZ boundary even at low strain amplitudes, whereas in the NZ middle, it took place only at high strain amplitudes. During cyclic deformation, the development of plastic deformation was clearly shown by the twinning band distribution at low strain amplitudes, which was characterized by two distribution modes (Figure 5(b)). This illustrates that the plastic deformation had two paths: one occurred in the region with the soft orientation (around the NZ/TMAZ boundary), and the other developed from the region with the soft orientation (around the NZ/TMAZ boundary) toward the region with the hard orientation (the NZ interior).

C. *Cyclic Stress–Strain Responses*

Figure 7 shows the typical hysteresis loops for the first cycle and mid-life cycle at the strain amplitude of

0.4 pct. For the PM at the first cycle (Figure 7(a)), the hysteresis loop was strongly asymmetric with the tensile stress much higher than the compressive stress, and the loop was significantly distorted at the compression region; this is attributed to the twinning–detwinning behavior.[31,32] For the PM at the mid-life cycle (Figure 7(b)), the asymmetric tensile and compressive stresses were still observed, but the loop was no longer distorted, which was consistent with previous studies[32] and might be related to the impediment of the twinning and detwinning processes with increasing cycles.[35] However, the hysteresis loops of the joints were quite different from those of the PM. At both the first cycle and mid-life cycle, the hysteresis loops were all asymmetric; the tensile stress was roughly equal to the compressive stress, and the loop was no longer distorted. This could be attributed to the nonuniform deformation of the joints (Figure 5), and the specific reason will be discussed in our next article.

Figure 8 shows the variation of the stress amplitude with the no. of cycles during cyclic deformation at different strain amplitudes for the PM, 800-rpm joint, and 3500-rpm joint. First, the stress amplitude increased with increasing the total strain amplitude. Second, the stress amplitude of the joints was lower than that of the PM at strain amplitudes higher than 0.2 pct. Third, the stress amplitudes at the higher rotation rate (3500 rpm) were larger than those at the lower one (800 rpm), which could be attributed to the relatively higher YS of the 3500-rpm joint.

At lower strain amplitudes, such as 0.1 and 0.2 pct for the PM, and 0.1 pct for the joints, the corresponding stress amplitudes were low and nearly constant during the entire cyclic deformation, indicating that no cyclic hardening appeared. It was noted that the stress
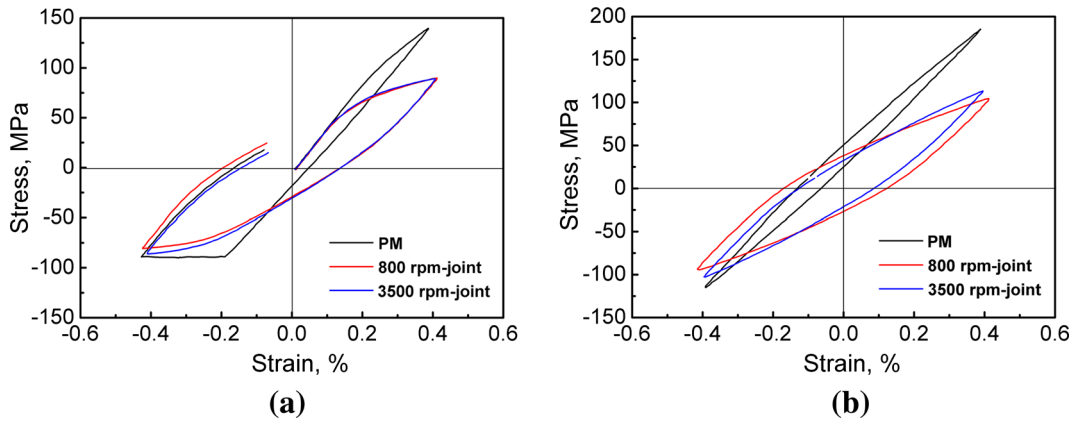
Fig. 7—Typical stress–strain hysteresis loops at a strain amplitude of 0.4 pct for (a) 1st cycle and (b) mid-life cycle.
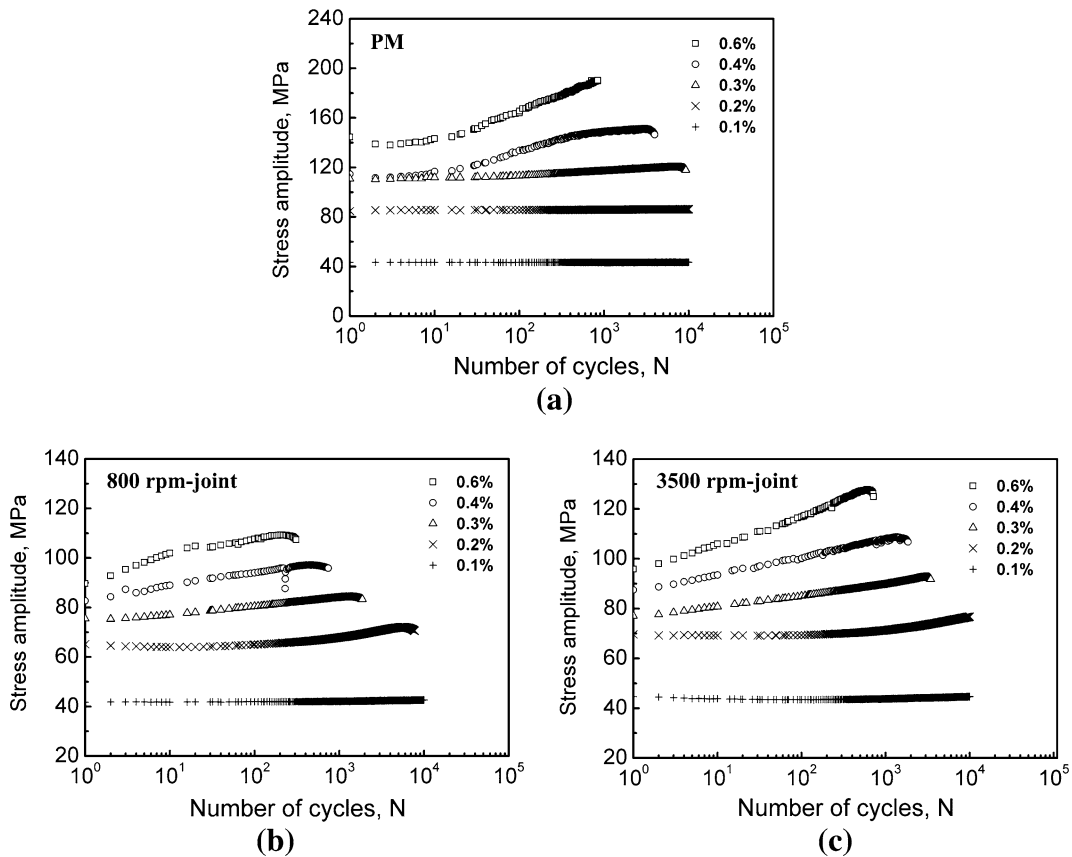
Fig. 8—Stress amplitude *vs* no. of cycles during cyclic deformation at different total strain amplitudes for (*a*) PM, (*b*) 800-rpm joint, (*c*) 3500-rpm joint.

amplitude of the joint was equal to that of the PM at the strain amplitude of 0.1 pct, but lower than that of the PM at strain amplitudes ranging from 0.2 to 0.6 pct. For the joints, as the strain amplitude increased to 0.2 pct, the stress amplitude remained stable for the initial 100 cycles and then increased gradually; a similar curve was observed for the PM at the stress amplitude of 0.3 pct. At higher strain amplitudes, the cyclic stress–strain responses were quite different between the PM and the joints. For the PM, the stress amplitude remained

constant during the initial cycles ranging from 10 to 20 at strain amplitudes from 0.4 and 0.6 pct, and then increased quickly as the cyclic deformation proceeded. However, for the joints, at strain amplitudes from 0.3 to 0.6 pct, the stress amplitude increased continuously as the cyclic deformation proceeded.

The variation of the plastic strain amplitude ($\Delta\varepsilon_p/2$) during cyclic deformation is shown in Figure 9. At lower strain amplitudes, such as 0.1 and 0.2 pct for the PM, and 0.1 pct for the joints, the plastic strain amplitudes
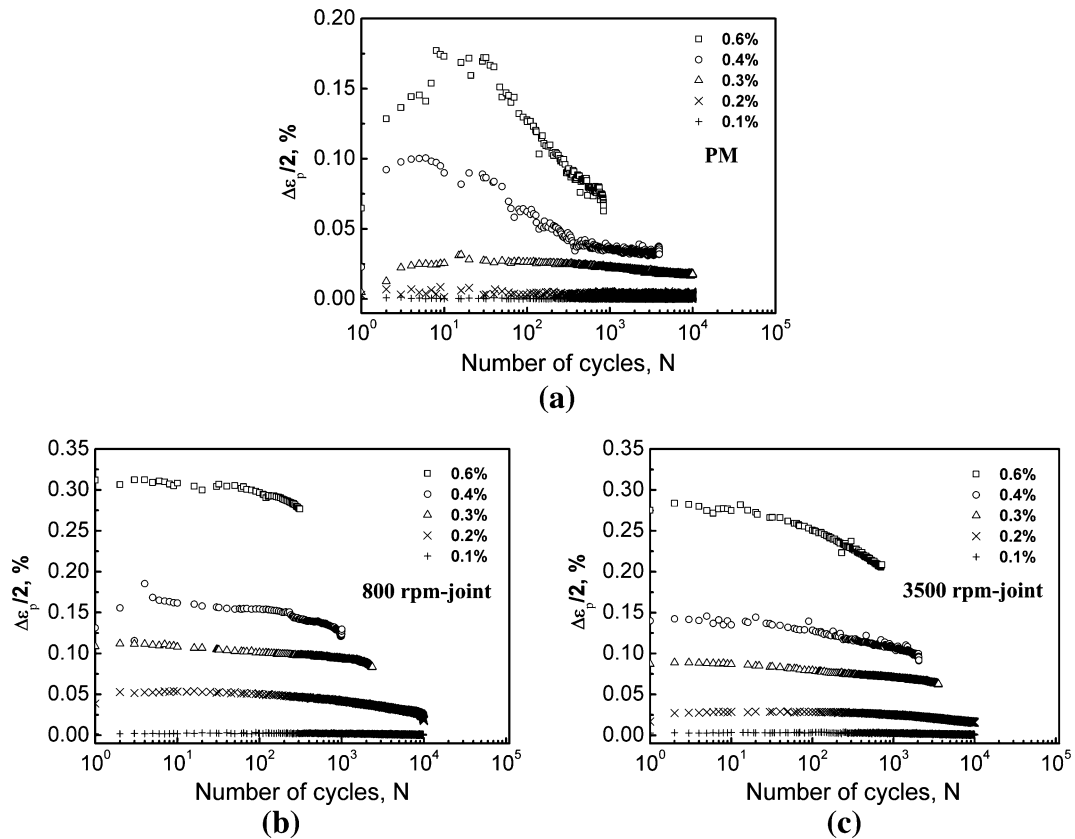
Fig. 9—Plastic strain amplitude *vs* no. of cycles during cyclic deformation at different total strain amplitudes for (*a*) PM, (*b*) 800-rpm joint, (*c*) 3500-rpm joint.

were stable as the cyclic deformation proceeded, indicating that neither cyclic softening nor cyclic hardening occurred. This result is consistent with the study of the extruded AZ31.[32,34,35] However, at the strain amplitude of 0.2 pct, higher plastic strain amplitudes were detected for the joints compared with the PM, and the plastic strain amplitude decreased as the cyclic deformation proceeded, indicating that the different deformations existed between the joints and the PM with cyclic hardening operating at the low strain amplitude for the joints.

At higher strain amplitudes, although the stress amplitude of the PM was always higher than that of the joints, their plastic strain amplitudes were the opposite. At strain amplitudes from 0.3 to 0.6 pct for the PM, and from 0.2 to 0.6 pct for the joints, the plastic strain amplitude of the 800-rpm joint was higher than that of the 3500-rpm joint, which was higher than that of the PM. In addition, different variations in the trends of the plastic strain amplitude *vs* the no. of cycles were observed between the PM and the joints. At strain amplitudes between 0.4 and 0.6 pct, the plastic strain amplitude of the PM increased significantly during the initial cycles ranging from 10 to 20, which was consistent with the platform of the stress amplitude, indicating that cyclic softening occurred; then, the plastic strain amplitude decreased gradually after 100 cycles, indicating that the cyclic hardening process appeared. This two-stage cyclic deformation was also found in another LCF study

of AZ31.[36] However, it is noticed that these phenomena disappeared in the FSW joints. At strain amplitudes from 0.3 to 0.6 pct, the plastic strain amplitudes of the joints decreased continuously as the cyclic deformation proceeded, indicating that only cyclic hardening occurred. Furthermore, similar curves of plastic strain amplitude were observed between the PM with the strain amplitude of 0.3 pct and the joints with the strain amplitude of 0.2 pct, which was consistent with the curves of stress amplitude.

The cyclic hardening phenomenon is characterized by the increase in the stress amplitude and the decrease in the plastic strain amplitude as the cyclic deformation proceeded. It was observed that the slopes in the stress amplitude or the plastic strain amplitude *vs* the no. of cycles were different between the joints and the PM. Thus, the following relationship was proposed to describe the change.[36,37]

$$\frac{\Delta \varepsilon_p}{2} = \alpha + \beta \log(N),\qquad [1]$$

where N is the no. of cycles during cyclic deformation, α is the initial plastic strain amplitude that corresponds to the 50th cycle for the PM, β is the slope that could be considered as a hardening coefficient. Both α and β depend on the applied strain amplitude.

Figure 10 shows the plot of the slope β as a function of the total strain amplitude for both the PM and joints. For the PM, β decreased gradually as the strain
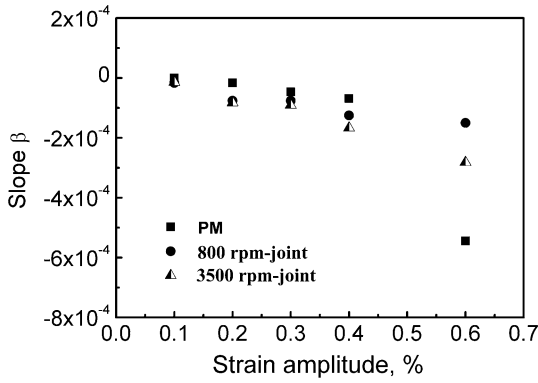
Fig. 10—Effect of applied strain amplitudes on slope β in Eq. [1].

Fig. 11—Variation of total strain amplitude as a function of no. of cycles to failure for PM and joints.

amplitude increased from 0.1 to 0.4 pct, and then it decreased sharply at 0.6 pct, which was consistent with other studies.[36,37] However, different variations of β were found in the joints. As the strain amplitude increased from 0.1 to 0.6 pct, β decreased linearly for both the 800-rpm joint and the 3500-rpm joint. This result is consistent with the variation of the plastic strain amplitude. When the strain amplitude was higher than 0.1 pct, the decrease rate of plastic strain amplitudes vs the no. of cycles remained almost constant. In addition, as the strain amplitude increased from 0.2 to 0.4 pct, the rate of decrease of the plastic strain amplitude vs the no. of cycles for the PM was lower than that for the joints (Figure 9) and thus, the corresponding β was higher. At 0.6 pct, the rate of decrease of the plastic strain amplitude vs the no. of cycles for the PM was much higher than that for the joints, resulting in a much lower β of the PM. Moreover, the rotation rate could influence β. The β of the 3500-rpm joint was lower than that of the 800-rpm joint and this trend was obvious at the strain amplitude of 0.6 pct.

As discussed above, the NZ/TMAZ boundary had the soft orientation and therefore, this region experienced plastic deformation first during the tension[22] and cyclic deformation. Compared with the PM, the plastic strain could occur on the NZ/TMAZ boundary for the joint under much lower stress. Therefore, at the strain amplitude of 0.2 pct, the plastic strain amplitude was measurable for the joints, while it was near zero for the PM. In addition, at the strain amplitude of 0.3 pct for the PM and 0.2 pct for the joints, the stress amplitude was lower. It is possible that little basal slip was activated during the initial 100 cycles, leading to little variation in the stress amplitude and plastic strain amplitude, and then the dislocation slip was accumulated and the twinning was activated, resulting in the cyclic hardening.

As the strain amplitude increased to 0.4 and 0.6 pct, two-stage cyclic hardening was observed for the PM, which was attributed to the strong rolling texture[36] and twinning during LCF.[38] However, for the joints, the cyclic deformation was mainly centered on the NZ/TMAZ boundary, because of the Schmid factor distribution (Figure 3(d)). Therefore, at strain amplitudes of 0.3 to 0.6 pct, both the dislocation slip and twinning
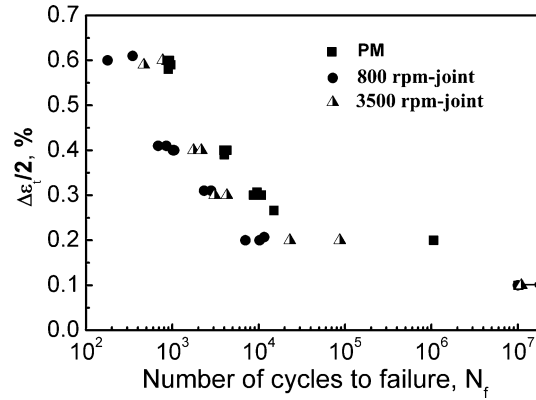
could be easily activated at the higher cyclic stress in this region and thus, cyclic hardening was observed at the early stage of cyclic deformation without the two-stage phenomenon. Moreover, in our previous studies, it was found that the basal texture on the NZ/TMAZ boundary could be weakened[14] and that the enlargement of the upper NZ with increasing the rotation rate could improve the strength of the joint.[22] Therefore, during cyclic deformation, the higher stress amplitude and lower plastic strain amplitude were obtained at the higher rotation rate.

D. Fatigue Life and LCF Parameters

Figure 11 shows the strain-life plot of the PM and the FSW joints. For most strain amplitudes the fatigue life of the PM was longer than that of the joints, and the life of the 3500-rpm joint was longer than that of the 800-rpm joint. In combination with the stress amplitude and plastic strain amplitude mentioned above, it can be concluded that the strain-controlled fatigue properties of the 3500-rpm joint are better than those of the 800-rpm joint.

The cyclic stress–strain curve could be described by the following equation:[39]

$$\frac{\Delta\sigma}{2} = K' \left(\frac{\Delta\varepsilon_p}{2}\right)^{n'}, \qquad [2]$$

where K' is the cyclic strength coefficient, n' is the cyclic strain hardening exponent, $\Delta\sigma/2$ and $\Delta\varepsilon_p/2$ are the stress amplitude and strain amplitude at the mid-life cycle, respectively. Through the linear fitting of $\log(\Delta\sigma/2) - \log(\Delta\varepsilon_p/2)$ (Figure 12(a)), the calculated K' and n' values according to Eq. [2] are given in Table II. During cyclic deformation, it seems that the cyclic strength coefficient and cyclic strain-hardening exponent increased from the 800-rpm joint to the 3500-rpm joint and obtained the highest values in the PM. Similar results were also reported for the FSW 6061Al by Feng et al.[21]

The total strain amplitude ($\Delta\varepsilon_t/2$) could be expressed as the elastic strain amplitude ($\Delta\varepsilon_e/2$) and plastic strain amplitude ($\Delta\varepsilon_p/2$), i.e.:
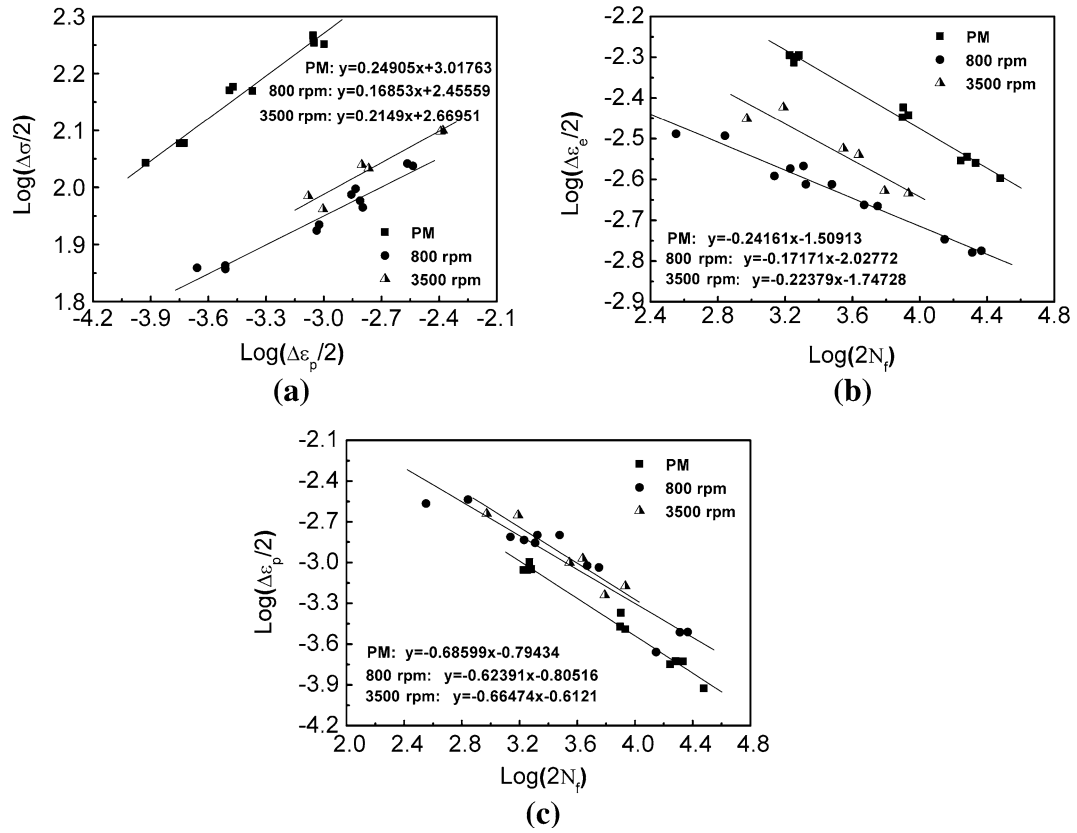
Fig. 12—Evaluation of fatigue parameters: (a) log stress amplitude vs log plastic strain amplitude at the half-life cycle, (b) log elastic strain amplitude vs log no. of cycles to failure, (c) log plastic strain amplitude vs log no. of cycles to failure.

Table II. Low-Cycle Fatigue Parameters for PM and FSW Joints

Low-Cycle Fatigue Parameters	PM	800-rpm Joint	3500-rpm Joint
Cyclic strain hardening exponent, n'	0.25	0.17	0.21
Cyclic strength coefficient, K' (MPa)	1041	285	467
Fatigue strength coefficient, σ'_f (MPa)	1393	422	805
Fatigue strength exponent, b	−0.24	−0.17	−0.22
Fatigue ductility coefficient, ε'_f	0.16	0.16	0.24
Fatigue ductility exponent, c	−0.69	−0.62	−0.66

$$\frac{\Delta\varepsilon_t}{2} = \frac{\Delta\varepsilon_e}{2} + \frac{\Delta\varepsilon_p}{2}. \quad [3]$$

The first part can be expressed by Basquin equation,

$$\frac{\Delta\varepsilon_e}{2} = \frac{\sigma'_f(2N_f)^b}{E}, \quad [4]$$

and the second term of Eq. [3] can be replaced by the Coffin–Manson relation,

$$\frac{\Delta\varepsilon_p}{2} = \varepsilon'_f(2N_f)^c \quad [5]$$

Then, Eq. [3] could be expressed as

$$\frac{\Delta\varepsilon_t}{2} = \frac{\sigma'_f(2N_f)^b}{E} + \varepsilon'_f(2N_f)^c, \quad [6]$$

where E is the Young's modulus (~45 GPa for the rolled AZ31), N_f is the fatigue life or no. of cycles to failure, σ'_f is the fatigue strength coefficient, b is the fatigue strength exponent, ε'_f is the fatigue ductility coefficient, and c is the fatigue ductility exponent. As shown in Figures 12(b) and (c), the relations between $\log(2N_f)$ and $\log(\Delta\varepsilon_e/2)$ and between $\log(2N_f)$ and $\log(\Delta\varepsilon_p/2)$ were analyzed by the linear fitting. The obtained experimental results indicated that fatigue deformation followed the Coffin–Mason and Basquin's equations well, and the estimated fatigue parameters based on Eq. [4] are summarized in Table II. It was found that the absolute values of all the fatigue parameters increased as the rotation rate increased.

E. Fractography

Macrographs of the cross sections of fractured fatigue joints are shown in Figure 13. All the fatigue cracks
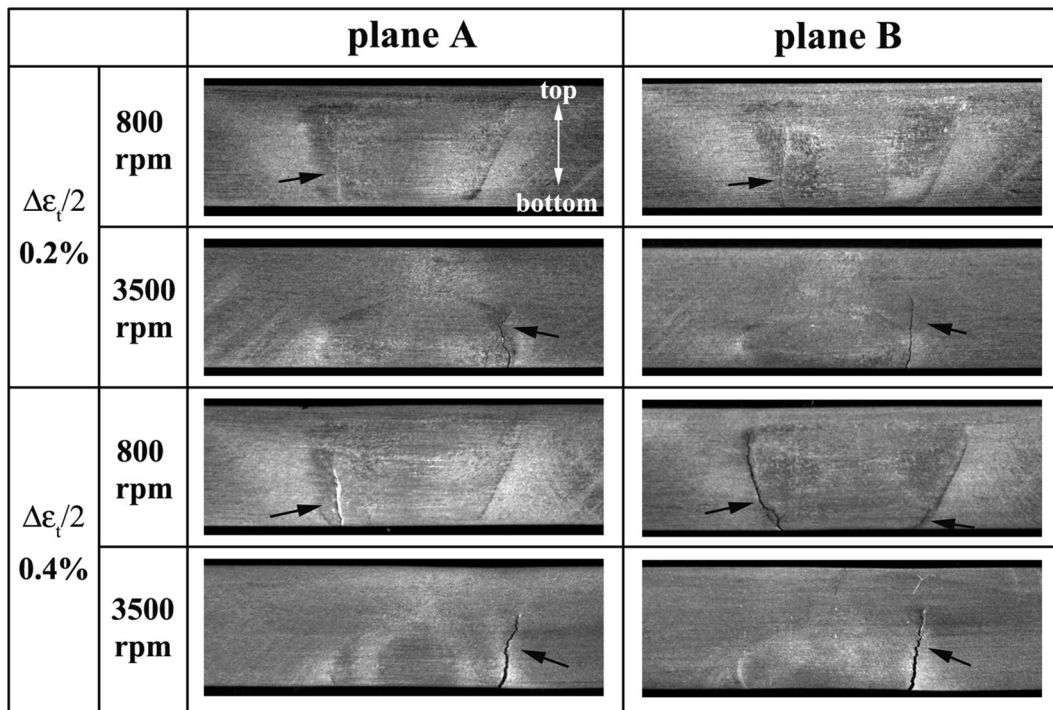
Fig. 13—Macrographs of failed LCF specimens at different strain amplitudes. Arrows show fatigue cracks.

initiated at the bottom of the joints and then propagated to the upper surface. Plane A and plane B are the two sides of a transverse tensile specimen, where the pin passed plane A earlier than plane B during the FSW process. At the low strain amplitude of 0.2 pct, all the specimens at different rotation rates failed in the NZ adjacent to the NZ/TMAZ boundary, with little difference between planes A and B. At the higher strain amplitude of 0.4 pct, the fracture locations varied at different rotation rates. The 3500-rpm joint failed at the NZ boundary on both planes A and B, with the crack propagating roughly along a straight line. However, the 800-rpm joint exhibited different fracture locations between planes A and B. The cracks were located at the NZ/TMAZ boundary on plane B, whereas it shifted to the NZ on plane A. A similar fracture mode was observed in the tension of the FSW AZ31 joint.[22]

At lower strain amplitudes, twinning bands were observed at the NZ/TMAZ boundary and adjacent NZ (Figure 5). A recent study revealed that the fatigue damage or crack occurring at twin boundaries depended on the crystallographic orientation and stacking fault energy;[40] however, the specific fatigue damage in the current study should be related to the unique grain orientation and twinning distribution of the FSW joint. Different from the uniform grain orientation distribution in the as-rolled pure Cu, Cu-Al, and Cu-Zn alloys,[40] and the as-extruded AZ31 alloy,[41] the grain orientation in the FSW joints had huge discrepancies around the NZ/TMAZ boundary (Figure 3), generating large local stress concentration around this position and forming twinning bands (Figure 5). As the strain amplitude increased, the local stress concentration around the twinning bands increased; once the microcracks were formed at the twin boundaries, these twinning bands could be favorable for the crack propagation.

At the lower strain amplitude, most twinning bands were produced in the adjacent NZ and were distributed consecutively (Figure 5). Therefore, at the strain amplitude of 0.2 pct, the joints failed in the NZ adjacent to the NZ/TMAZ boundary for both the 800-rpm joint and 3500-rpm joint.

As the strain amplitude increased to 0.4 pct, more twinning bands were produced at the NZ/TMAZ boundary because of more serious nonuniform deformation, and the twinning bands also developed in the adjacent NZ. Therefore, the fracture path, which was along the NZ/TMAZ boundary on plane B and along the adjacent NZ on plane A, was not a straight line for the 800-rpm joint. Moreover, the joint was enhanced by the enlargement of the upper NZ at 3500 rpm,[22] and therefore, the fracture location was the same for both planes A and B, which was similar to the tensile fracture behavior of the FSW AZ31 joints.[22]

Figure 14 shows the overall fracture surfaces of the PM and joints at strain amplitudes between 0.2 and 0.4 pct. The fatigue process can be divided into three stages: crack initiation, crack propagation, and final fast fracture. Three corresponding regions were obvious at low strain amplitudes, while the crack propagation region was significantly reduced at high strain amplitudes. For both the PM and the FSW joints, the fatigue cracks all initiated at the surface of the specimens, which is consistent with other studies.[42–44] For Mg alloys, the surface crack initiation is associated with the fracture of precipitates,[43] the crack of the grain and twin boundaries,[41] and the crack along the slip bands.[35]
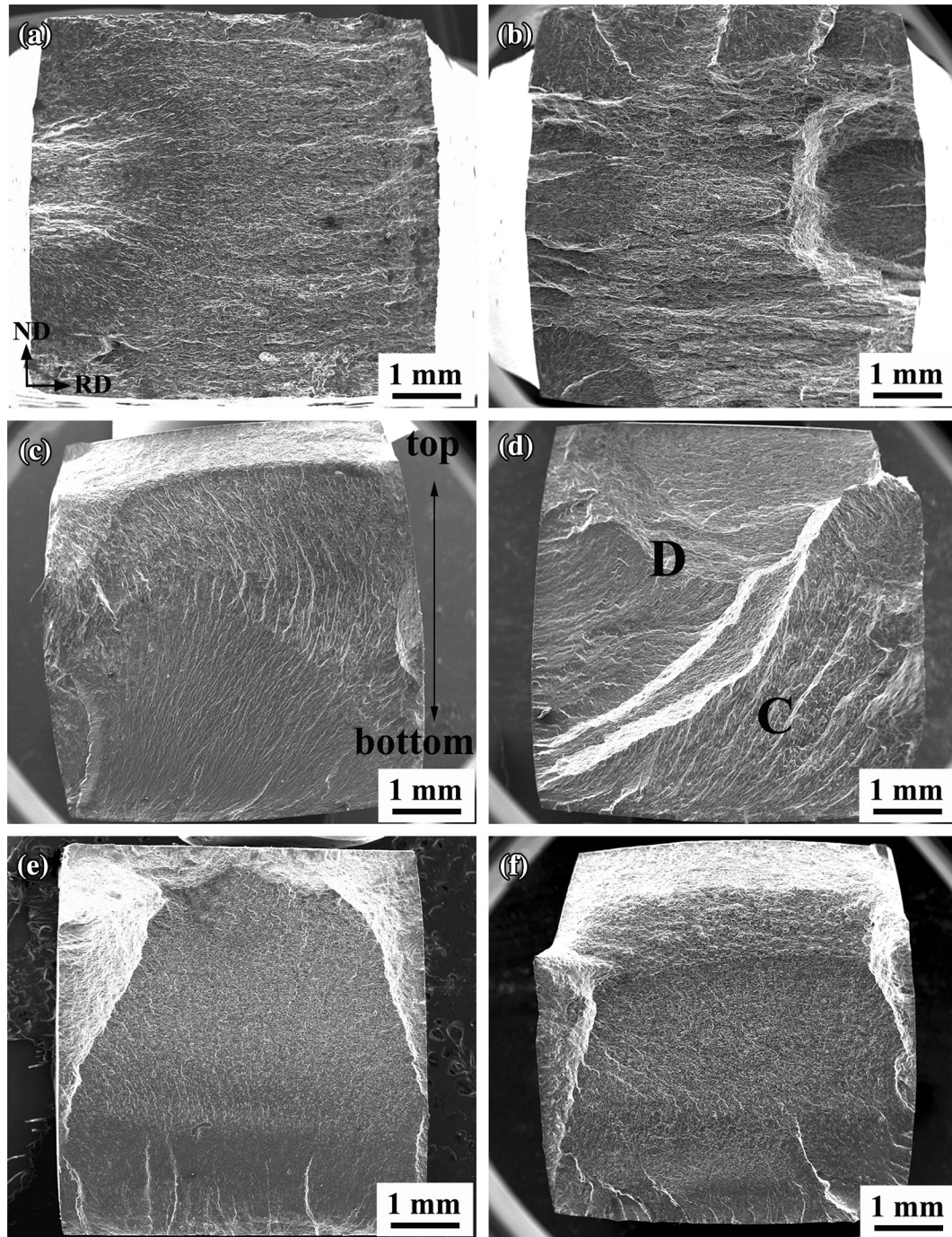
Fig. 14—SEM images of overall fracture surfaces at $\Delta\varepsilon_t/2 = 0.2$ pct for (*a*) PM, (*c*) 800-rpm joint, (*e*) 3500-rpm joint, and at $\Delta\varepsilon_t/2 = 0.4$ pct for (*b*) PM, (*d*) 800-rpm joint, (*f*) 3500-rpm joint.

The fracture surfaces showed different morphologies under different strain amplitudes. For the PM, the fracture surface was flat and only one crack initiation was detected at 0.2 pct strain amplitude (Figure 14(a)), while the surface was very rough and more crack initiations were found at 0.4 pct strain amplitude (Figure 14(b)). Similar facture surfaces were observed in both the 800-rpm joint and the 3500-rpm joint at 0.2 pct strain amplitude (Figures 14(c) and (e)); the crack initiation was located on the bottom surface and consistent with the macrograph in Figure 13. As the

strain amplitude increased to 0.4 pct, some differences were observed on the fracture surfaces at different rotation rates. A large step was observed on the fracture surface of the 800-rpm joint (Figure 14(d)), which divided the fracture surface into two parts (regions C and D). These two regions correspond to the different macrocrack propagation paths on planes A and B (Figure 13). The fatigue cracks initiated at the NZ/TMAZ boundary and propagated along region C, which corresponds to the macrocrack on plane B (Figure 13); and finally, the specimen fractured in the NZ (region D),
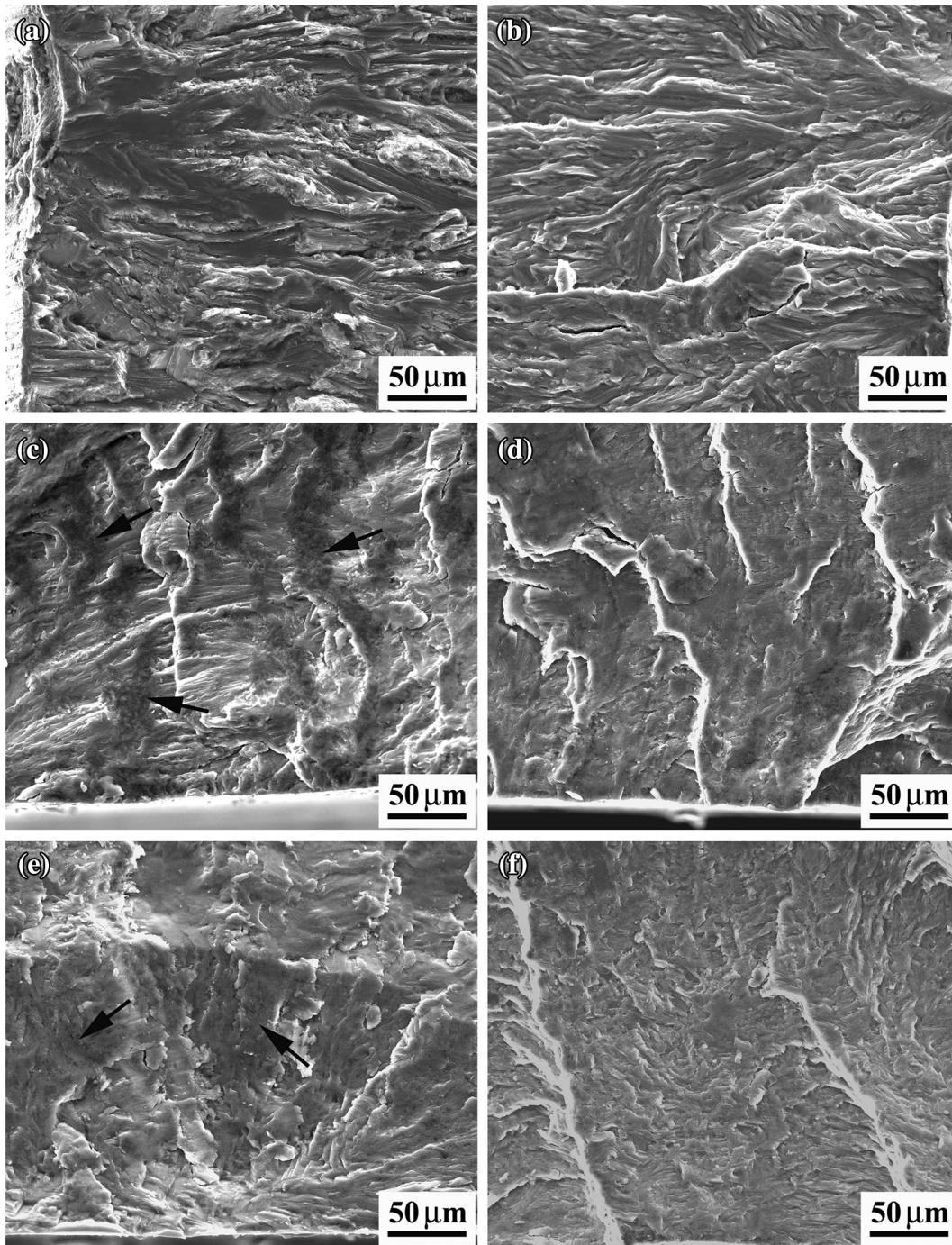
Fig. 15—SEM fractographs near crack initiation at $\Delta\varepsilon_t/2$ = 0.2 pct for (*a*) PM, (*c*) 800-rpm joint, (*e*) 3500-rpm joint, and at $\Delta\varepsilon_t/2$ = 0.4 pct for (*b*) PM, (*d*) 800-rpm joint, (*f*) 3500-rpm joint.

which corresponds to the macrocrack in plane A (Figure 13). Compared with the 800-rpm joint, the facture surface was flatter for the 3500-rpm joint at 0.4 pct strain amplitude (Figure 14(f)), which could be attributed to the enlargement of the upper NZ. In addition, for the 3500-rpm joint, the crack also initiated at the bottom of the NZ/TMAZ boundary, which is consistent with the macrograph of the fracture location in Figure 13. Moreover, the crack propagation region was smaller than that at the strain amplitude of 0.2 pct.

The SEM images of crack initiations are shown in Figure 15. For the PM, small facets and steps were observed with the direction of steps consistent with the direction of crack propagation. Some researchers[44,45] suggested that this crack propagation mode was transgranular cracking. These facets were large and flat at the lower strain amplitude (Figure 15(a)) and small and rough at the higher strain amplitude (Figure 15(b)), which could be attributed to the difference in the no. of cycles experienced.
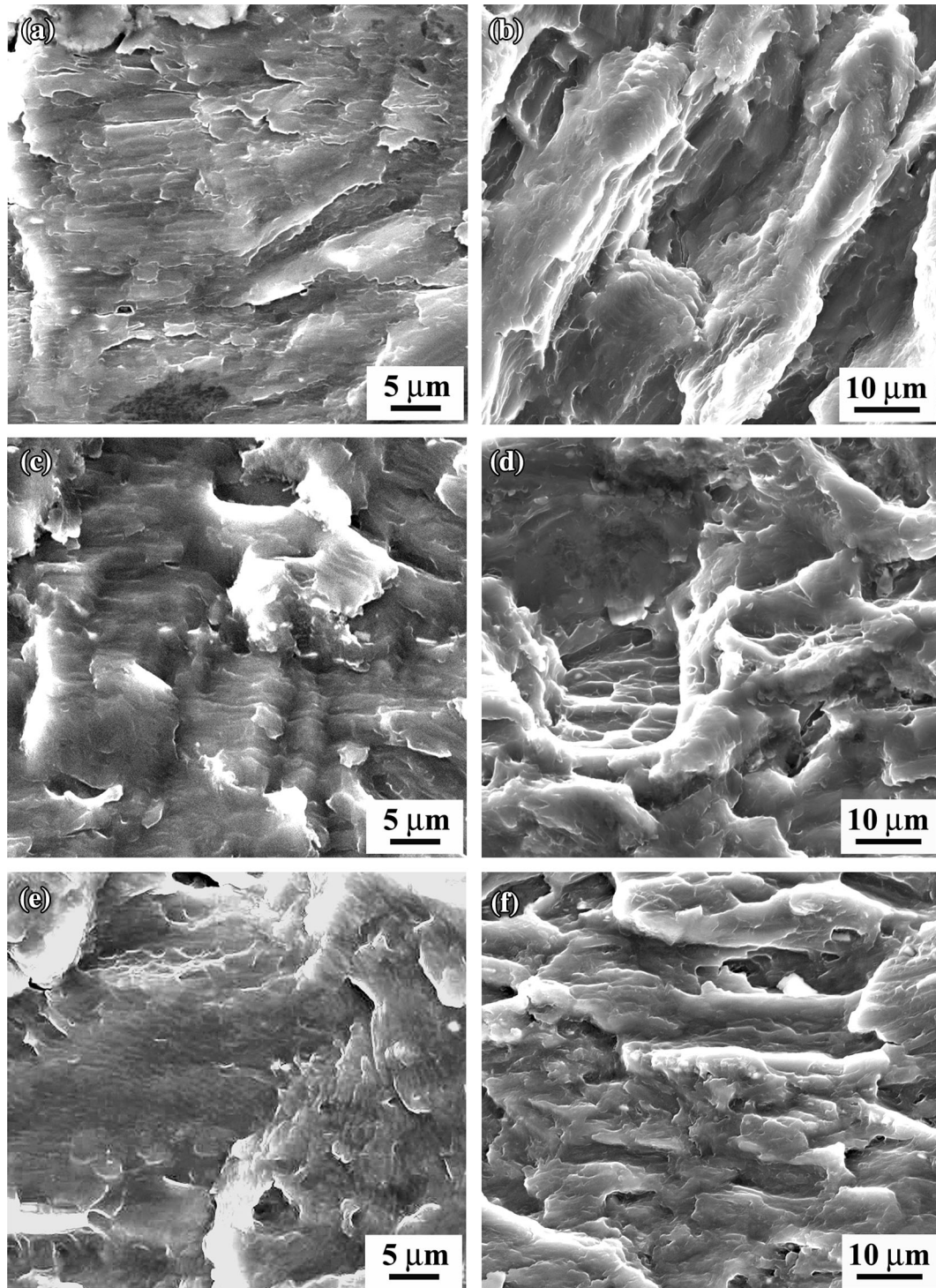
Fig. 16—SEM fractographs showing crack propagation region at $\Delta\varepsilon_t/2 = 0.2$ pct for (*a*) PM, (*c*) 800-rpm joint, (*e*) 3500-rpm joint, and at $\Delta\varepsilon_t/2 = 0.4$ pct for (*b*) PM, (*d*) 800-rpm joint, (*f*) 3500-rpm joint.

Figures 15(c) and (d) show the typical crack initiations of the joint (at 800 rpm) at strain amplitudes between 0.2 and 0.4 pct. As discussed above, these regions are prone to basal slip because of the soft orientation. Consequently, the fracture surfaces were smoother with larger facets and smaller steps compared with the PM, indicating cleavage fracture. At a strain amplitude of 0.2 pct, some black regions (shown by

black arrows) with higher oxygen content were observed in the crack initiation regions (Figure 15(c)), which could be attributed to the oxidation during the cyclic deformation. At the higher strain amplitude of 0.4 pct, no obvious oxides were detected on the fracture surface because of the short fatigue life (Figure 15(d)). Figures 15(e) and (f) show the crack initiations for the 3500-rpm joint. Similar to the 800-rpm joint, the

fracture surface was also flat for the 3500-rpm joint, indicating cleavage fracture; and the black regions (shown by black arrows) with oxidation were observed at a strain amplitude of 0.2 pct, but no black regions were found at a strain amplitude of 0.4 pct.

Figure 16 shows the SEM images of the crack propagation regions. At a low strain amplitude of 0.2 pct, the fracture surface was characterized by the typical fatigue striations and some secondary cracks (Figures 16(a), (c) and (e)), which is consistent with a previous study.[32] The fatigue striations normally occurred by a repeated plastic blunting—sharpening process in face-centered cubic materials because of the slip of dislocations in the plastic zone at the fatigue crack tip.[46,47] Begum et al.[36,38] considered that the formation of the fatigue striations in the extruded Mg alloy was related to the twinning in the compression and detwinning in the tension during cyclic deformation.[48,49] Because each fatigue striation normally represents a single cycle,[39] the spacing of fatigue striations of the PM was smaller than that of the joints due to the higher fatigue live of the PM. As the strain amplitude increased to 0.4 pct, the fatigue lives were significantly decreased for both the PM and the joints, so that fatigue striations disappeared (Figures 16(b), (d) and (f)). In addition, in contrast with the PM, some dimples were observed on the fracture surfaces of the joints (Figures 16(d) and (f)), indicating the fast fatigue crack propagation, which was consistent with the lower fatigue lives of the joints.

IV. CONCLUSIONS

1. Sound FSW joints of 6.4-mm-thick rolled AZ31 plates were realized at rotation rates of 800 and 3500 rpm, producing joint efficiencies (UTS_{joint}/UTS_{PM}) of 70 and 85 pct, respectively. As the rotation rate increased from 800 to 3500 rpm, a basin-shaped NZ changed to a two-layer-structured NZ with the upper NZ nearly equal to the lower NZ.
2. Equiaxed grains were observed in the NZ of the 800-rpm joint and the lower NZ of the 3500-rpm joint; however, the upper NZ of the 3500-rpm joint exhibited elongated grains with the different texture that led to the increased tensile strength of the joint. The middle of the NZs exhibited a hard orientation, while a soft orientation was observed in the region around the NZ/TMAZ boundary.
3. At the strain amplitude of 0.1 pct, the FSW joints owned a fatigue life similar to that of the PM. Meanwhile, the fatigue resistance of the FSW joints was slightly improved as the rotation rate increased from 800 to 3500 rpm. The obtained fatigue data for the PM and FSW joints can be well described using the Coffin–Manson and Basquin's relationships.
4. FSW affected the cyclic behavior of the rolled AZ31 plate greatly. While asymmetric loops were observed for the PM, the FSW joints exhibited symmetric hysteresis loops.
5. At a given strain amplitude, especially a higher strain amplitude, the FSW joints had a lower stress amplitude, a higher plastic strain amplitude, and a lower fatigue life than the PM. At higher strain amplitudes, although two-stage cyclic hardening characteristics were observed in the PM, the FSW joints exhibited variations that were almost linear.
6. At the low strain amplitude of 0.1 pct, $\{10\bar{1}2\}$ twins were observed only in the region around the NZ/TMAZ boundary. The twinning was activated along the NZ/TMAZ boundary and then propagated to the NZ interior. As the strain amplitude increased to 0.4 pct, some $\{10\bar{1}2\}$ twins were detected in the NZ middle.
7. For the FSW joints, the fatigue cracks initiated at the bottom of the joints and propagated along the NZ/TMAZ boundary or the NZ adjacent to the NZ/TMAZ boundary, depending on the total strain amplitudes and the rotation rate.

REFERENCES

1. R.S. Mishra and Z.Y. Ma: *Mater. Sci. Eng. A*, 2005, vol. 50, pp. 1–78.
2. W. Woo, H. Choo, D.W. Brown, P. K. Liaw, and Z. Feng: *Scripta Mater.*, 2006, vol. 54, pp. 1859–64.
3. S.H.C. Park, Y.S. Sato, and H. Kokawa: *Metall. Mater. Trans. A*, 2003, vol. 34A, pp. 987–94.
4. W. Yuan, R.S. Mishra, B. Carlson, R.K. Mishra, R. Verma, and R. Kubic: *Scripta Mater.*, 2011, vol. 64, pp. 580–83.
5. J.S. Liao, N. Yamamoto, and K. Nakata: *Metall. Mater. Trans. A*, 2009, vol. 40A, pp. 2212–19.
6. S. Mironov, Q. Yang, H. Takahashi, I. Takahashi, K. Okamoto, Y.S. Sato, and H. Kokawa: *Metall. Mater. Trans. A*, 2010, vol. 41A, pp. 1016–24.
7. U.F.H.R. Suhuddin, S. Mironov, Y.S. Sato, H. Kokawa, and C.W. Lee: *Acta Mater.*, 2009, vol. 57, pp. 5406–18.
8. W. Woo, H. Choo, M.B. Prime, Z. Feng, and B. Clausen: *Acta Mater.*, 2008, vol. 56, pp. 1701–11.
9. L. Commin, M. Dumont, J.E. Masse, and L. Barrallier: *Acta Mater.*, 2009, vol. 57, pp. 326–34.
10. J. Yang, B.L. Xiao, D. Wang, and Z.Y. Ma: *Mater. Sci. Eng. A*, 2010, vol. 527, pp. 708–14.
11. W.B. Lee, Y.M. Yeon, and S.B. Jung: *Mater. Sci. Technol.*, 2003, vol. 19, pp. 785–90.
12. S. Lin, S. Kim, C.G. Lee, C.D. Yim, and S.J. Kim: *Metall. Mater. Trans. A*, 2005, vol. 36A, pp. 1609–12.
13. N. Afrin, D.L. Chen, X. Cao, and M. Jahazi: *Mater. Sci. Eng. A*, 2008, vol. 472, pp. 179–86.
14. J. Yang, D. Wang, B.L. Xiao, and Z.Y. Ma: 8th *International Friction Stir Welding Symposium*, 2010, pp. 1–11.
15. M.A. Gharacheh, A.H. Kokabi, G.H. Daneshi, B. Shalchi Amirkhiz, and R. Sarrafi: *Int. J. Mach. Tool Manuf.*, 2006, vol. 46, pp. 1983–87.
16. M. Tsujikawa, H. Somekawa, K. Higashi, H. Iwaskai, T. Hasegawa, and A. Mizuta: *Mater. Trans.*, 2004, vol. 45, pp. 419–22.
17. S.M. Chowdhury, D.L. Chen, S.D. Bhole, and X. Cao: *Fatigue*, 2010, pp. 825–33.
18. G. Padmanaban and V. Balasubramanian: *Mater. Des.*, 2010, vol. 31, pp. 3724–32.

19. G. Padmanaban, V. Balasubramanian, and G.M. Reddy: *J. Mater. Process. Technol.*, 2011, vol. 211, pp. 1224–33.
20. A.H. Feng, D.L. Chen, and Z.Y. Ma: *Metall. Mater. Trans. A*, 2010, vol. 41A, pp. 957–71.
21. A.H. Feng, D.L. Chen, and Z.Y. Ma: *Metall. Mater. Trans. A*, 2010, vol. 41A, pp. 2626–41.
22. J. Yang, B.L. Xiao, D. Wang, and Z.Y. Ma: *Metall. Mater. Trans. A*, 2013, vol. 44A, pp. 517–30.
23. S.H.C. Park, Y.S. Sato, and H. Kokawa: *Scripta Mater.*, 2003, vol. 49, pp. 161–66.
24. S. Xu and X. Deng: *Acta Mater.*, 2008, vol. 56, pp. 1326–41.
25. X.X. Zhang, B.L. Xiao, and Z.Y. Ma: *Metall. Mater. Trans. A*, 2011, vol. 42A, pp. 3229–39.
26. T.A. Samman, X. Li, and S.G. Chowdhury: *Mater. Sci. Eng. A*, 2010, vol. 527, pp. 3450–63.
27. Z. Zhang, M.P. Wang, N. Jiang, and S. Zhu: *J. Alloy. Compd.*, 2012, vol. 512, pp. 73–78.
28. J. Scott, M. Miles, D. Fullwood, B. Adams, A. Khosravani, and R.K. Mishra: *Metall. Mater. Trans. A*, 2013, vol. 44A, pp. 512–16.
29. S.L. Couling, J.F. Pashak, and L. Sturkey: *Trans. ASM*, 1958, vol. 51, pp. 94–107.
30. R.L. Xin, B. Li, A.L. Liao, Z. Zhou, and Q. Liu: *Metall. Mater. Trans. A*, 2012, vol. 43A, pp. 2500–08.
31. S.H. Park, S.G. Hong, W. Bang, and C.S. Lee: *Mater. Sci. Eng. A*, 2010, vol. 527, pp. 417–23.
32. X.Z. Lin and D.L. Chen: *Mater. Sci. Eng. A*, 2008, vol. 496, pp. 106–13.
33. M. Gotting and B. Scholtes: *Int. J. Mater. Res.*, 2006, vol. 97, pp. 1378–83.
34. S. Begum, D.L. Chen, S. Xu, and A.A. Luo: *Mater. Sci. Eng. A*, 2009, vol. 517, pp. 334–43.
35. F. Lv, F. Yang, Q.Q. Duan, Y.S. Yang, S.D. Wu, S.X. Li, and Z.F. Zhang: *Int. J. Fatigue*, 2011, vol. 33, pp. 672–82.
36. S. Begum, D.L. Chen, S. Xu, and A.A. Luo: *Int. J. Fatigue*, 2009, vol. 31, pp. 726–35.
37. U. Noster and B. Scholtes: *Z. Metallk.*, 2003, vol. 94, pp. 559–63.
38. S. Begum, D.L. Chen, S. Xu, and A.A. Luo: *Metall. Mater. Trans. A*, 2008, vol. 39A, pp. 3014–24.
39. G.E. Dieter: *Mechanical Metallurgy*, 3rd ed., McGraw-Hill, New York, 1986.
40. Z.J. Zhang, P. Zhang, L.L. Li, and Z.F. Zhang: *Acta Mater.*, 2012, vol. 60, pp. 3113–27.
41. F. Yang, S.M. Yin, S.X. Li, and Z.F. Zhang: *Mater. Sci. Eng. A*, 2008, vol. 491, pp. 131–36.
42. L.J. Chen, C.Y. Wang, W. Wu, Z. Liu, G.M. Stoica, L. Wu, and P.K. Liaw: *Metall. Mater. Trans. A*, 2007, vol. 38A, pp. 2235–41.
43. K. Gall, G. Biallas, H.J. Maier, P. Gullett, M.F. Horstemeyer, and D.L. McDowell: *Metall. Mater. Trans. A*, 2004, vol. 35A, pp. 321–31.
44. K. Tokaji, M. Kamakura, Y. Ishiizumi, and N. Hasegawa: *Int. J. Fatigue*, 2004, vol. 26, pp. 1217–24.
45. T.S. Shih, W.S. Liu, and Y.J. Chen: *Mater. Sci. Eng. A*, 2002, vol. 325, pp. 152–62.
46. G.E. Dieter: *Mechanical Metallurgy*, McGraw-Hill Series, McGraw-Hill, New York, 1986.
47. C. Laird: *Fatigue Crack Propagation*, ASTM STP 415, ASTM, West Conshohocken, PA, 1967, pp. 131–68.
48. L. Wu, A. Jain, D.W. Brown, G.M. Stoica, S.R. Agnew, B. Clausen, D.E. Fielden, and P.K. Liaw: *Acta Mater.*, 2008, vol. 56, pp. 688–95.
49. Y.N. Wang and J.C. Huang: *Acta Mater.*, 2007, vol. 55, pp. 897–905.